Sedimentation of a single soluble particle at low Reynolds and high Péclet numbers

Nan He, Yutong Cui, David Wai Quan Chin, Thierry Darnige, Philippe Claudin, Benoît Semin

To cite this version:

Nan He, Yutong Cui, David Wai Quan Chin, Thierry Darnige, Philippe Claudin, et al.. Sedimentation of a single soluble particle at low Reynolds and high Péclet numbers. Physical Review Fluids, 2024, 9, pp.044502. 10.1103/PhysRevFluids.9.044502 . hal-04266598v2

HAL Id: hal-04266598
https://hal.sorbonne-universite.fr/hal-04266598v2

Submitted on 5 Nov 2024

Sedimentation of a single soluble particle at low Reynolds and high Péclet numbers

Nan He (何楠),[*] Yutong Cui (崔于桐), David Wai Quan Chin, Thierry Darnige, Philippe Claudin, and Benoît Semin[†]
PMMH, CNRS, ESPCI Paris, Université PSL, Sorbonne Université,
Université Paris Cité, F-75005, Paris, France

(Dated: 2024 年 11 月 5 日)

摘要

We investigate experimentally the dissolution of an almost spherical butyramide particle during its sedimentation, in the low Reynolds high Péclet regime. The particle sediments in a quiescent aqueous solution, and its shape and position are measured simultaneously by a camera attached to a translation stage. The particle is tracked in real time, and the translation stage moves accordingly to keep the particle in the field of the camera. The measurements from the particle image show that the radius shrinking rate is constant with time, and independent of the initial radius of the particle. We explain this with a simple model, based on the sedimentation law in the Stokes' regime and the mass transfer rate at low Reynolds and high Péclet numbers. The theoretical and experimental results are consistent within 20%. We introduce two correction factors to take into account the non-sphericity of the particle and the inclusions of air bubbles inside the particle, and reach quantitative agreement. With these corrections, the indirect measurement of the radius shrinking rate deduced from the position measurement is also in agreement with the model. We discuss other correction factors, and explain why they are negligible in the present experiment. We also compute the effective Sherwood number as a function of an effective Péclet number.

I. INTRODUCTION

The mass transfer from a solid soluble particle in a fluid is of major relevance in chemical engineering [1], for example in food industry [2] and in pharmaceutical industry [3, 4]. Mass transfer from particles associated to phase change also occurs in a geophysical context, for instance the melting of rocks in magma [5, 6], the sublimation of ice drops in the atmosphere [7], or the melting of snow and hail when reaching a sea [8].

The dynamics of dissolution is different for isolated particle and for a suspension of particles. In the latter case, the particles interact through the concentration of the solute in the fluid phase, and due to the hydrodynamic interaction between the particles [9]. Moreover, the dissolution of the particle can affect the density of the fluid phase, inducing buoyancy effects like the formation of plumes. In the present article we focus on the case of an isolated particle whose dissolution does not change the density of the surrounding fluid.

The diverse environments where mass transfer involving soluble particles takes place are categorized into distinct regimes. This classification is based on the two main dimensionless parameters that predominantly control the mass transfer from a single spherical particle.Following many previous studies, we choose to use the Reynolds number $\mathrm{Re} = \rho_f aU/\eta$ which characterises the flow regime, and the Péclet number $\mathrm{Pe} = aU/D$ which characterises the mass transfer regime. In the previous definitions, a is the particle typical size (the radius for a sphere), U its settling velocity, η is the dynamic viscosity of the fluid, ρ_f its mass density, and D is the diffusion coefficient of the solute composing the particle into the fluid. An alternative to Pe is to use the Schmidt number Sc, where these three numbers are related by $\mathrm{Pe} = \mathrm{Re} \times \mathrm{Sc}$. The Schmidt number is known to play an important role in the dissolution process [10]. Both Re and Pe vanish for a motionless particle, for which the mass transfer is only due to molecular diffusion. In gases, these two numbers are usually similar, whereas in liquids the Péclet number is several orders of magnitudes higher than the Reynolds number. The third relevant

---

[*] nan.he@espci.fr

[†] benoit.semin@espci.fr

dimensionless number in this context is the Sherwood number Sh, which quantifies the mass transfer and is defined as the ratio between the total mass transfer and its purely diffusive component for the same particle (an expression of the Sherwood number for our case is given later in equation (5). Many past studies have performed experiments, numerical simulations, or developed models, to relate Sh (the result) to Re and Pe (the control parameters). This approaches is valid if the chemical kinetic of dissolution is fast, like in the present article. Otherwise, a new dimensionless number should be taken into account, for example the Damköhler number which compares the dissolution rate coefficient to a characteristic diffusion velocity [10]. Finally, in order to better cover the subject, it is also important to consider heat transfer from a particle, which is analogous to mass transfer within some hypotheses, in particular negligible radiation. It means that dissolution processes are very similar to melting processes. In the case of heat transfer, the analog to Pe is the thermal Péclet number defined with the thermal diffusivity, the equivalent to Sc is the Prandtl number Pr, and the equivalent to Sh is the Nusselt number Nu.

The first regime is when both Re and Pe are small. It has for example been recently investigated experimentally by [11], measuring the size of an almost spherical succinic acid particle in unstirred water as a function of time. The results are compatible with a purely diffusive mass transfer (i.e. $\mathrm{Sh} = 1$ with our definition). The diffusive mass transfer has also been verified experimentally in the case of a droplet of hexadecane levitated in an eletrodynamic balance and undergoing a flow of N_2 and helium [12]. Since the fluids are at rest, the expected result is similar for a liquid or a solid particle in this regime.

The regime we are particularly interested in this work is the case of small Re and large Pe, which, as we already said, is possible in a liquid. A fundamental analytical calculation for a sphere has been performed by [13], which gives $\mathrm{Sh} \propto \mathrm{Pe}^{1/3}$. This scaling law has been confirmed by numerical simulations [14, 15] as well as experiments using two rotating cylinders to impose an homogeneous flow and electrochemical measurements to obtain the mass flux [16]. A similar configuration is the sinking of small spheres in a turbulent flow, which has been investigated experimentally and numerically by [17].

Finally, many experiments and simulations have been performed in the regime where both Re and Pe are large, for a fixed particle submitted to a uniform flow or a free falling particle. In this case, one expects the scaling law $\mathrm{Sh} \propto \mathrm{Re}^{1/2}\mathrm{Sc}^{1/3}$ [18], and most of the results are effectively compatible with a correlation $\mathrm{Sh} \propto \mathrm{Re}^{1/2}\mathrm{Sc}^{\alpha}$, α is in the range 0.3–0.4, plus correction terms. Using numerous simulations, [19] have found $\alpha = 0.36$ in the case of heat transfer for $3 \times 10^{-3} < \mathrm{Pr} < 10^{1}$ and $10^{2} < \mathrm{Re} < 5 \times 10^{4}$. The experiments include various systems: sedimentation and dissolution of urea spheres in a vertical glass column [20], dissolution of benzoic acid spheres in a flow (natural or forced convection) of water or propylene glycol [21], dissolution of ice ball in a hydrodynamic channel with water flow [22], dissolution of hard candy submitted to a flow [23]. However, some other experimental configurations with a very different flow, like large ice balls melting in a turbulent von Kármán flow [24], leads to different scalings.

Spherical versus non-spherical particles have also been studied in this large Re-Pe regime. One can in particular mention experiments on the dissolution of neutrally buoyant particles with rectangular cuboid initial shapes in isotropic turbulent environments [25]. Numerically, simulations of heat transfer past spheres, cuboids and ellipsoids been performed by [26], and empirical correlation for non-spherical ellipsoids have been obtained by [27–30]. Finally, several correction factor to the mass transfer, associated with the aspect ratio of non-spherical particles, the thermal effect due to dissolution, and the finite solubility effect have been discussed in [15, 31].

In the present work, we investigate the dissolution of an almost spherical particle that sediments in an aqueous solution at rest. These experiments belong to the low Reynolds and high Péclet regime, which, in comparison to the high Reynolds regime, has been less studied. In the next section 2, we present the theoretical framework that we need to interpret the results, showing in particular that we expect a constant reduction rate of the particle size. We describe the experimental setup in section 3 which allows us to measure simultaneously the position and the shape of the particle during its sedimentation. We emphasise the use of particles made of butyramide, a chemical which does not change the density of water when dissolving, hence preventing any buoyancy effect in the fluid. Section 4 is devoted to the comparison of our experimental results with the model, and we show that we can make it quantitative accounting for shape and density correction factors. Finally, conclusions and perspectives are drawn in section 5. Technical details such as the fabrication of the particles, the behavior of their settling velocity, and the measurements of relevant parameters are comprehensively documented in the supplementary material (including references [32–38]).

II. THEORY FOR A SPHERICAL PARTICLE

We present in this section the theory of a spherical particle of radius a falling in a quiescent fluid. We focus on the regime for which the particle Reynolds number is low – this is consistent with our experiments for which Re in the range $0.3 - 0.8$. It means that the fluid motion around the particle are well described by the Stokes equations, where the fluid inertia can be neglected. The particle velocity then results from the balance of the three relevant forces: the downward force of gravity F_g, the upward buoyant force F_b, and the drag force F_d, which classically express as:

$$F_g = \frac{4}{3}\pi a^3 \rho_p g, \tag{1}$$

$$F_b = \frac{4}{3}\pi a^3 \rho_f g, \tag{2}$$

$$F_d = 6\pi\eta a U. \tag{3}$$

ρ_p is density of the particle and g is gravity acceleration. The resulting settling velocity of the particle is:

$$U = \frac{2}{9}\frac{(\rho_p - \rho_f)g}{\eta}a^2. \tag{4}$$

This particle can dissolve in the fluid, and we assume that it does so in the regime where its Péclet number is large (in the range $300 - 1000$ in our experiment). Both small Re and large Pe are encountered for small soluble particles in liquids as one typically has $D \ll \eta/\rho_f$ (Parameters can be found in Table I). In this regime, we follow the analytical calculations derived by [13] for a perfect sphere with the approximation of a thin concentration boundary layer around the particle. It yields the mass transfer equation predominated by convection as $\dot{m} \simeq 8Dac_0\mathrm{Pe}^{1/3}$, where c_0 represents the concentration (in kg/m^3) of the dissolved matter closest to the particle, which is the saturated concentration of the solute. The derivation also assumes no change of fluid density, small solute concentration, isothermal dissolution, hypotheses which will be discussed later in the text. Moreover, the viscosity in this model is assumed to be the one of the solution far from the particle. Given the large Schmidt number, the size of the concentration boundary layer ($\propto D/U$) where the concentration of solute is significant is indeed much smaller than the size over which the velocity field varies (radius size $\propto a$).

Given that pure diffusion mass transfer rate for sphere is represented by $\dot{m} = 4\pi Dac_0$, the total mass transfer rate $\dot{m}$ of the particle in our experiments, i.e. the mass the particle losses per unit time when is dissolves, can be expressed in terms of the Sherwood number as:

$$\mathrm{Sh} = -\frac{\dot{m}}{4\pi Dac_0} \simeq \frac{2}{\pi}\mathrm{Pe}^{1/3}, \tag{5}$$

where the dot denotes time derivative.

Relating the mass of the sphere to its radius $m = \frac{4}{3}\pi\rho_p a^3$, the mass transfer rate can also be written as:

$$\dot{m} = 4\pi\rho_p a^2\dot{a}. \tag{6}$$

Equating $\dot{m}$ in (5) and (6), while making explicit the expression of the Péclet number and substituting U from (4), we finally obtain

$$\dot{a} = -\frac{2}{\pi}\left(\frac{2}{9}\right)^{\frac{1}{3}}\frac{D^{\frac{2}{3}}c_0}{\rho_p}\left(\frac{(\rho_p-\rho_f)g}{\eta}\right)^{\frac{1}{3}}. \tag{7}$$

All factors on the right hand side of the above expression only depend on the characteristics of the fluid and the particle. The rate at which the particle size decreases over time is thus constant, i.e. independent of the radius of the particle, resulting in a linear relationship between a and t. We will test this remarkably simple behaviour experimentally in the present article.

III. EXPERIMENTAL SET-UP

We have built an experiment to investigate the dynamics of such a particle that sediments and continuously dissolves, resulting in a reduction of its size and mass. The setup consists in an elongated tank and a particle tracking system, as illustrated in Fig. 1. The tank has a square cross-section, with an inner width of 10 mm and an inner length of 150 mm. As the particles we consider are rather small (on the order of 100 µm), and thus easily disturbed by small velocity fluctuations, the tank is placed in a larger water bath, also with a square cross-section (internal width of 30 mm), to avoid convective disturbances inevitably caused by small temperature differences between the two sides of the experiment. The transparency of the two tanks allows for visual observation of the particle sedimentation process. The reliability of the entire experimental device has been verified through the sedimentation of plastic beads in distilled water. The two tanks are joined at the top by a detachable connector to ensure the verticality of the inner tank and prevent temperature fluctuations in the water bath caused by evaporation. In the present study, a camera with a resolution of 1936 × 1216 pixels, manufactured by IDS industrial camera company, was used. Prior to the experiments, careful scale calibration was performed, with a typical resolution of 5 pixels/µm. The particle tracking was controlled by a self-written Labview program, inspired by [39]. The camera was connected to a computer to measure in real-time the position of the particle in the image, enabling to move the linear stage from PI (Physical Instrument) and therefore the camera to follow the particle. Thus, synchronous position information and images of the particle were obtained from the tracking system.

The density of the aqueous solution containing the dissolved matter from the solid particle is usually larger than that of the pure water – this is the case for NaCl for example. Here we use particles of butyramide, a chemical whose saturated solution has a density very close to that of pure water, which minimise the effect of density increase around the particle during its sedimentation-dissolution motion. At 21 °C, the typical temperature at which experiments were run, we indeed measured with a pycnometer and a precision scale that the density of the saturated butyramide is $0.998 \pm 0.001 \mathrm{g\,cm^{-3}}$, i.e. similar to the density of water at the same temperature (see Table I). Butyramide is also very soluble in water [35], and the crystals have a bulk density of $1.032\,\mathrm{g\,cm^{-3}}$. The theory is simple for perfect spheres only. However, preparing spherical particles for this experiment is a challenge because butyramide crystals naturally tend to form plate-like shapes when cristallisation occurs in solution. In order to reproducibly get butyramide particles with an aspect ratio close to unity, we extract them from a layer of solid butyramide obtained by melting the crystals in a beaker, forming a homogeneous solid layer once cooled back to room temperature. As discussed below, this protocole also allows us to minimize the presence of air bubbles inside the particles. Using a stainless steel tip with an inner diameter of around 1 mm provide particles in the right range of size for our experiment, whose shape are typically like rounded cylinders. Additional details on the particle fabrication process are available in Section I of the supplementary material.

Before the experiment is started, two different fluid layers are prepared in the tank. The upper layer labelled layer I in schematics of Fig. 1 is a saturated butyramide solution in which the particle cannot dissolve. The lower layer (layer III) is water with a bit of dissolved NaCl, in order to make it slightly heavier than the upper layer, for stability. The amount of NaCl is such that the density of this lower layer is $1.014\,\mathrm{g\,cm^{-3}}$. The upper layer thus does not contain NaCl, and the lower layer does not contain butyramide. We assume that this moderate presence of NaCl does not influence the dissolution process of butyramide in water. Once prepared, the two solutions are first put in a vacuum pump to remove air bubbles before being placed in the experimental tank. At the beginning of the experiment, pure water at room temperature is injected into the water bath. The sedimentation tank is then carefully placed and attached by the detachable connector. After the NaCl solution is poured at the bottom of the tank, the saturated butyramide is carefully injected using a syringe with a small-sized tip, providing a more stable flow. This process results in a thin middle transition layer (layer II in Fig. 1) of intermediate concentration of butyramide and NaCl that appears due to diffusion, and the interface between the upper and lower layers can be visually distinguished. The vertical thickness of the lower layer solution is 95 mm, and that of the upper layer solution is 45 mm. Butyramide particles that have been pre-stocked in a saturated solution are drawn into a syringe without a tip, and this syringe is then placed vertically on top of the tank. At this point, the saturated solutions in the syringe and in the tank are connected and the particles can start to sediment. Once a particle is in the field of view of the camera, the tracking system captures it immediately, and track it until its size becomes smaller than $\simeq 3\,\mu\mathrm{m}$.

Moreover, the different physical parameters involved in this experiment have been carefully measured or determined. Their values are shown in Table I. The dynamic viscosities of the saturated butyramide and NaCl solutions were measured with high precision using a rheometer Anton Paar specifically for liquids with a viscosity similar to water. The saturated butyramide concentration c_0 is well calibrated as a function of temperature in [35]. For the diffusivity D, we recorded with a camera the refraction angle of the interface of a stratified solution consisting of a saturated butyramide solution and still water over time. D was deduced from the square relationship between the maximum reflected angle and time. More details about these measurements can be found in the supplementary material.

Particle	Saturated butyramide solution				NaCl solution		Water
ρ_p	D	c_0	ρ_f	η	ρ_f	η	ρ_f
$\mathrm{g\,cm^{-3}}$	$\mathrm{m^2\,s^{-1}}$	$\mathrm{g\,cm^{-3}}$	$\mathrm{g\,cm^{-3}}$	mPa s	$\mathrm{g\,cm^{-3}}$	mPa s	$\mathrm{g\,cm^{-3}}$
1.032	7.2×10^{-10}	0.182	0.998	1.853	1.014	1.018	0.9980
	$\pm 0.4 \times 10^{-10}$	± 0.005	± 0.001	± 0.002	± 0.001	± 0.006	± 0.0001

表 I. Parameters of the experiment at 21 ± 0.5 °C. The column about water is given for comparison.

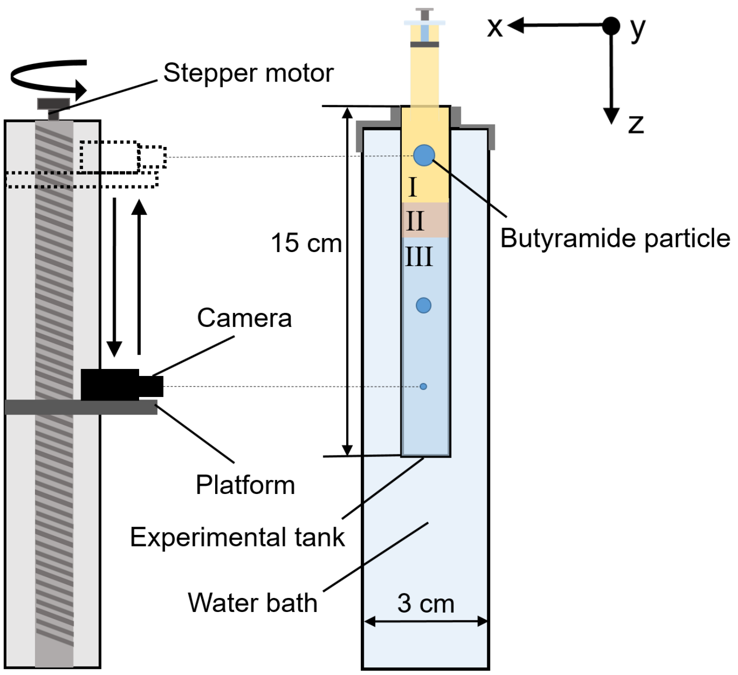

图 1. Schematic diagram of the experimental set-up. In the tank, the upper layer I is saturated butyramide and the lower layer III is the NaCl aqueous solution. The transition layer is numbered II.

IV. RESULTS AND DISCUSSION

A. Simultaneous measurements of radius and position of the particle

Figure 2 illustrates the dissolution process of the particle during its sedimentation. We observe that the particle shrinks over time, gradually rounding off into a shape slightly elongated in the vertical direction. We can also notice a slight rotation of the particle. More quantitatively, we estimated the volume change of the particle by image analysis: binarising the picture of the particle with a suitable gray threshold and finding boundaries after convex hull, which fills the holes inside of binarised image, we could extract a projected area of the particle. From that surface, a centroid, which we take as the effective location z of the particle, and an equivalent radius a can be defined (Fig. 2, bottom line). Following these quantities picture after picture, we could this way measure z and a as functions of time, as displayed in figure 3.

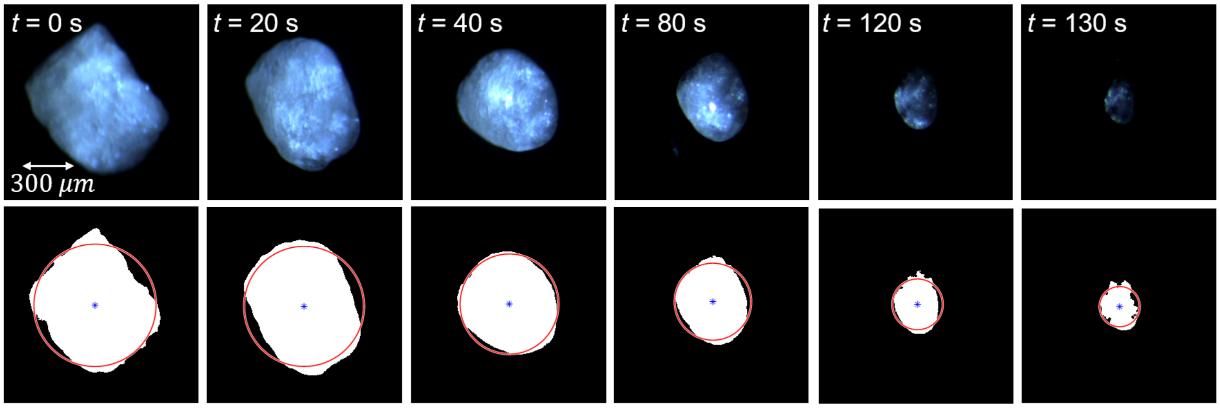

图 2. Dissolving process of the particle over time. The top line shows the original pictures, as captured by the camera during the experiment. The bottom line shows the corresponding processed images, where the white area A, obtained after convex closure of the binarised picture, represents the projected surface of the particle. On each of these bottom images, the blue-star point indicates the centroid of the white area, and the red circle, centred on that point, has the same surface as the white area, i.e. gives the equivalent radius $a = \sqrt{A/\pi}$ of the particle.

After the particle is released from the syringe, it first sediments in the upper layer composed of a saturated butyramide solution. During this period (stage I), as the particle does not dissolve, its equivalent radius remains constant. Slight fluctuations can however be observed, caused by the rotation of the particle. By taking the average particle radius during this stage, the initial particle radius, denoted as a_0, can be obtained. The settling velocity of the particle also remains constant, and an initial value U_0 can be similarly computed from the average slope of the particle vertical displacement $z(t)$. With these initial values a_0 and U_0, which are the maximal radius and velocity of the particle during the sedimentation, we can evaluate the maximal Reynolds number of the particle by $\mathrm{Re} = a_0 U_0 \rho_f / \eta$. Across all experimental runs, the average value of Re is found to be 0.5 (in the range $0.3 - 0.8$).

At time $t = t_0$ the particle enters the transition layer where the upper-layer butyramide and lower-layer NaCl solutions are mixing by diffusion. In this thin transition layer the stratification causes a significant drop of the particle settling velocity associated with an enhanced drag [32]. During this stage II, the particle begins to dissolve, and it does so with an almost constant radius shrinking rate. At time $t = t_1$ the particle has reached the lower layer and its velocity corresponds again to sedimentation in homogeneous solution (additional details on velocity are provided in Fig. B of the supplementary material). As shown in Fig. 3(a), throughout its sedimentation in this lower layer (stage III) the particle equivalent radius continues to decrease at a constant rate, which is consistent with the theoretical expectation (7). A linear fitting of the data $a(t)$ in this stage gives a direct measurement of the radius shrinking rate, denoted as $\dot{a}_1$. We shall see below that this shrinking rate can be also estimated in another way, and will be denoted as $\dot{a}_2$.

Simultaneously, the particle velocity continuously decreases and notably reaches zero at some time t_{up}, after which the particle motion is reversed, see Fig. 3(b). This is due to some air bubbles trapped inside the particle during its preparation. As we detail in the following analysis, we will need to account for the fact that the effective density of the particle must be corrected by a factor β_b, associated with the presence of these bubbles. As the density difference $\rho_p - \rho_f$ is small, even a value of β_b close to unity has a significant quantitative effect. Of course, such a constant correction factor cannot reproduce the particle motion reversal. Instead, close to that moment t_{up}, the volume of the bubbles V_b inside the particle can be assumed constant, so that, as the particle matter further dissolves, its effective density becomes less than that of the surrounding fluid solution and it eventually rises. One can one then can compute V_b at that reversing time with

$$V_b\left(\rho_p - \rho_g\right) = \frac{4}{3}\pi\left(\rho_p - \rho_f\right)a^3(t = t_{\mathrm{up}}), \tag{8}$$

where $\rho_g = 1.2 \times 10^{-3}\ \mathrm{g\,cm^{-3}}$ is the air density. Notice that, interestingly, the value of the rate $\dot{a}$ remains unchanged during the rising stage. We define the time t_2 at which V_b represents 1% of the overall particle volume. Later analysis will then be restricted to times between t_1 and t_2, so that the effect of these bubbles in the particle sedimentation is small, a part a corrective factor for the particle bulk density.

The radius shrinking rate can be alternatively obtained from the particle position. As $\dot{a}$ is a constant (Eq. 7), a in the expression of the settling velocity U (Eq. 4) can then be replaced by $a = a_1 + \dot{a}(t - t_1)$, where $a_1 = a(t_1)$. Integrated once, the vertical position of the particle thus writes

$$z = \int_{t_1}^{t} U dt' = \frac{2}{9}\frac{(\rho_p - \rho_f)g}{\eta}\left[\frac{1}{3}\dot{a}^2(t - t_1)^3 + a_1\dot{a}(t - t_1)^2 + a_1^2(t - t_1)\right] + z_1, \tag{9}$$

where the z_1 is particle vertical position at the beginning of stage III (time t_1). Fitting this expression to the data $z(t)$ allows us to get a value of $\dot{a}$, which we denote as $\dot{a}_2$ to distinguish with the more direct estimate $\dot{a}_1$. Both values are presented in Fig. 4. Importantly, in this fitting process, two other parameters are determined by fit: a_1 and z_1. The precision on fitting parameters is good (the maximal error bar for $\dot{a}_2$ is $\pm 0.05\ \mathrm{\mu m\,s^{-1}}$), and we have for instance checked that imposing a_1 from the measurement $a(t)$ in the fitting of $z(t)$ leads to consistent results.

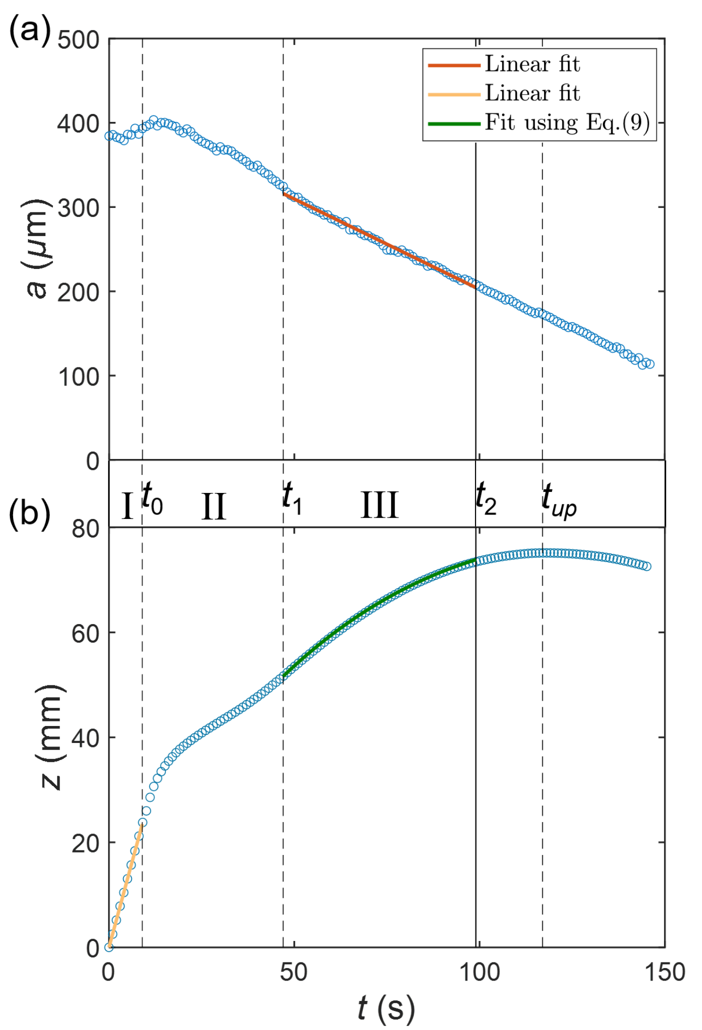

图 3. Time evolution of the equivalent radius a. (a) and the vertical displacement z (b) of the particle. Blue circles: experimental data. The vertical dashed lines show the times separating the different stages: t_0 end of the saturated layer, t_1 end of the transition layer, t_{up} motion reversal. Those times were determined using the velocity deduced from the derivative of the displacement (b), see Fig. B in supplementary material. Solid black line: time before which the volume of the air bubbles attached to the particle is less than 1%. Red line: linear fit in stage III of the radius decrease to deduce $\dot{a}_1$. Yellow line: linear fit in stage I of the particle position to deduce U_0. Green curve: fit of $z(t)$ in stage III with Eq. 9, from which another estimate $\dot{a}_2$ of the radius shrinking rate is obtained.

B. Radius shrinking rate $\dot{a}$

As theoretically expected and showed in Fig. 4, we find both $\dot{a}_1$ and $\dot{a}_2$ constant, i.e. independent of the initial size a_0 of the particle. The prediction from (7) is above the $\dot{a}_1$ measurements by 20%. Moreover, although on the same order, $\dot{a}_2$ is systematically smaller than $\dot{a}_1$ by a factor of $\simeq 2$. These discrepancies prompt us to revisit the above theoretical expressions in order to understand where the idealised case of a homogeneous spherical particle we have considered must be corrected. We have already mentioned in the previous section that the presence of trapped air bubbles must be accounted for with an effective particle density corrected by a factor β_b. Another important aspect is the geometry of the particle. Since we have only access to a projection of the particle shape, it is unlikely that the effective radius a we have introduced quantitatively works for the particle volume. However, this volume is key for the computation of the gravity and buoyancy forces. To account for this volume uncertainty, we introduce a correction factor β_a that will multiply the radius in the expression of these forces. We discuss later in section IV C why we do not introduce additional correction factors for the other variables. With these two correction factors β_a and β_b, the expressions for U, $\dot{a}$ and z rewrite

$$U = \frac{2}{9}\frac{(\beta_b\rho_p - \rho_f)g}{\eta}\beta_a^3 a^2, \tag{10}$$

$$\dot{a} = -\frac{2}{\pi}\left(\frac{2}{9}\right)^{\frac{1}{3}}\frac{D^{\frac{2}{3}}c_0}{\beta_a^2\beta_b\rho_p}\left(\frac{(\beta_b\rho_p - \rho_f)g}{\eta}\right)^{\frac{1}{3}}, \tag{11}$$

$$z = \int_{t_1}^{t} U dt' = \frac{2}{9}\frac{(\beta_b\rho_p - \rho_f)g}{\eta}\beta_a^3\left[\frac{1}{3}\dot{a}^2(t-t_1)^3 + a_1\dot{a}(t-t_1)^2 + a_1^2(t-t_1)\right] + z_1. \tag{12}$$

Using the data in stage I (upper layer), where U_0 and a_0 are measured accurately and for which the density as well as the viscosity of saturated butyramide are known, (10) gives a first relationship between the correction factors β_a and β_b. Similarly, with the linear fit of the radius reduction in stage III (lower layer) giving the rate $\dot{a}_1$, layer in which the density, the viscosity as well as the diffusivity of butyramide in water are known, (11) gives a second relationship linking β_a and β_b. They can be solved numerically, and, upon ensemble averaging over 13 independent experimental runs, we obtained $\beta_a = 0.921 \pm 0.002$ and $\beta_b = 0.988 \pm 0.002$. With these values, the fit of the curve $z(t)$ in stage III with (12) allows us to deduce a new value of $\dot{a}_2$. As shown in Fig. 4, the theoretical prediction of $\dot{a}$ now fits the direct measurements $\dot{a}_1$ as it should, and the corrected $\dot{a}_2$ are now quantitatively consistent with $\dot{a}_1$. Importantly, these corrections assume that these factors can be taken constant over the whole sedimentation process (in fact, until time t_2).

A value of β_b so close to unity may seem surprising, but because we are dealing with a small density difference between particle and fluid, these numerical adjustments are very sensitive. In fact, trying to impose $\beta_b = 1$ (resp. $\beta_a = 1$), we were not able to reach a quantitative matching of $\dot{a}_1$, $\dot{a}_2$ and theory as in Fig. 4 playing with β_a (resp. β_b) only. Furthermore, the value we got for β_a corresponds to an actual volume of the particle about 3/4 times smaller than deduced from the surface-induced effective radius a. This is consistent with particles in the form of an ellipsoid with its major axis parallel to the vertical, as observed in the experiments (see supplementary material).

C. Other correction factors

Other correcting factors could of course be considered. First of all, if ellipsoid-shaped particles are at play, the drag force is modified by the particle aspect ratio E, defined as the ratio between the major and the minor axes lengths. Following the work of [38] for spheroids, the Stokes drag correction factor for a motion parallel to the major axis follows the relation

$$\beta_{\text{drag}} = \left(\frac{4}{5} + \frac{E}{5}\right)E^{-1/3}. \tag{13}$$

The analysis of the pictures of the sedimenting particles shows aspect ratios typically between 1 and 2, with an average around 1.3 (see supplementary material). This corresponds to a drag correction factor

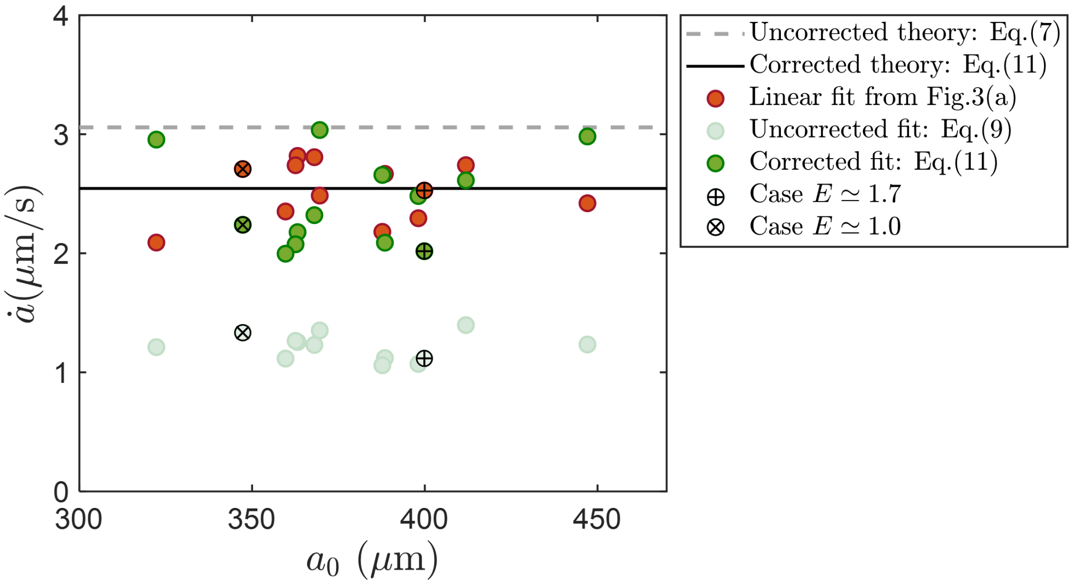

图 4. Reduction rate of the particle radius $\dot{a}$ from theory and data analyses for various initial particle size a_0. Red dots: direct measurement from the linear fitting of $a(t)$ (see Fig. 3a). These are what we denoted as $\dot{a}_1$. Green dots: indirect values obtained from the fitting of $z(t)$ (see Fig. 3b). These are what we denoted as $\dot{a}_2$. Light green points: fitting without any correction factors, i.e. using Eq. 9. Dark green points: fitting accounting for correction factors, i.e. using Eq. 12. Gray dash line: uncorrected theory (7). Black solid line: corrected theory (11). Circles with plus and cross symbols represent the experimental cases where the particle aspect ratio E respectively averages around 1.7 and 1 over $t_1 - t_2$, see also section IV C. These values correspond to the cases illustrated in Fig. H(b) and (c) of the supplementary material. Data dispersion shows the overall precision we can reach, but from the fitting process of a single experimental run, error bars are smaller than the symbol size.

$\beta_{\text{drag}} \simeq 0.97$. Accounting for it in the force balance, the above analysis of the particle's dynamics is not significantly affected: variations by less than a percent are found for β_a and β_b, and around 1% for $\dot{a}$. At the first order, this shape effect on the drag can then be ignored for the present problem. Furthermore, as observed in Fig. 4, the cases with $E \simeq 1.7$ and $E \simeq 1.0$ exhibit nearly identical $\dot{a}$ values, whether it is the direct measurement $\dot{a}_1$ or the indirectly derived value $\dot{a}_2$. This further substantiates that the impact of shape variation during the dissolution process on the $\dot{a}$ is of second order in importance.

The shape of the particle influences its mass and heat transfer processes as well. The heat transfer from a particle is analogous to mass transfer within some hypotheses, in particular when radiation is negligible. We use the work of [29] that provides Nusselt numbers for ellipsoids across a wide range of aspect ratios, E. Here with Re $\simeq 0.5$ and Sc $\simeq 1300$, which are typical values of these experiments, we obtain a correction factor $\beta_m \simeq 1.008$ for the Sherwood number Sh when the particle aspect ratio is between $E = 1.3$ and $E = 1$. Including this correction factor into the theoretical framework has a negligible impact on the results. Similarly to the case addressed in the previous paragraph, we find deviations of less than 1% in β_a, β_b and $\dot{a}$.

The theory of [13] which gives Eq. (5) for the scaling law relating the Sherwood number to the Péclet number, relies on the hypotheses that the concentration of the solute is infinitesimal, and that there is no thermal effects during the dissolution. These two assumptions are not verified for butyramide: the solubility of butyramide is large, and its dissolution in water is endothermic [35]. We can evaluate the corresponding correction factor $\beta_{\rm sol}$ using the results of [31]. These results are valid in the case of high Péclet and Schmidt numbers, which is the regime of the present experiments. The actual Sherwood number is then the one given by Eq. (5) multiplied by the factor:

$$\beta_{\rm sol} = \frac{1}{\gamma^{-1} - J^{2/3}/K}. \tag{14}$$

In this expression γ is a correction factor introduced by [31] to take into account the finite solubility and $J^{2/3}/K$ accounts for the non-isothermal effects during the dissolution. We estimate $\gamma = 1.09$ for butyramide using a linear fit from the data of table 2 in [31]. J is ratio of the molecular diffusivity D of the solute by the thermal diffusivity of the liquid α. Its value for water is $\alpha = 1.45 \times 10^{-7}$ $\mathrm{m^2\,s^{-1}}$ [40]. $K = c_p/dL$ is a dimensionless number involving the specific heat of the liquid c_p, the latent heat of absorption L and a coefficient d, which is the slope of the relationship of the concentration and temperature. For water, the specific heat is $c_p = 4.15\,\mathrm{kJ\,kg^{-1}\,K^{-1}}$, $d = 0.01$ $\mathrm{K^{-1}}$ and $L = -400\,\mathrm{kJ\,kg^{-1}}$, as reported from the measurements by [35]. The positive value of d implies that heat absorbed during butyramide dissolution results in a decrease of the interfacial temperature and equilibrium concentration. The value of the correction factor $\beta_{\rm sol}$ only slightly changes from 1.057 to 1.062 when evaluated based for a NaCl solution, so that we can take $\beta_{\rm sol} \simeq 1.06$. Incorporating this value into our theoretical analysis does not affect much the results, with, as in the above paragraph, variations by less than a percent are found for β_a and β_b, and around 1% for $\dot{a}$. This correction can thus be neglected at first order for the present analysis.

D. Effective Péclet and Sherwood numbers

These experimental data finally allow us to assess the scaling law relating the Sherwood to the Péclet numbers (5). Because we do not directly measure $\dot{m}$ but the grain size reduction rate $\dot{a}$ instead, we rather define an effective Sherwood-like number as:

$$\tilde{\mathrm{Sh}} = \beta_a \beta_b \, \frac{\rho_p a \dot{a}}{D c_0}. \tag{15}$$

For a spherical particle, for which $\dot{m}$ and $\dot{a}$ are simply related (Eq. 6), and setting the corrective factors $\beta_{a,b}$ to unity, both definitions of Sh and $\tilde{\mathrm{Sh}}$ coincide. Here, we not only wish to express this number with quantities we have direct access to, but also aim at accounting for the corrections we have discussed above. Consequently, we write the effective Péclet number as

$$\tilde{\mathrm{Pe}} = \beta_a \, \frac{U a}{D} \tag{16}$$

It can be directly estimated along each experimental run, also accounting for the radius correction. Plotting $\tilde{\mathrm{Sh}}$ as a function of $\tilde{\mathrm{Pe}}$ for all of our data clearly provides the expected increasing trend (Fig. 5). The inset of Fig. 5 where the same data are displayed in log-log scale confirms that they verified the power law of Eq. (5) with a 1/3 exponent. Data scattering is important, on the order of 30%, which is similar to what is displayed in Fig. 4. For comparison to theory, $\tilde{\mathrm{Sh}}$ is computed with U and $\dot{a}$ from their corrected expressions (10) and (11), setting the factors to the experimentally-determined averaged values $\beta_a = 0.921$ and $\beta_b = 0.988$, and where a is deduced from $\tilde{\mathrm{Pe}}$ with (16). The agreement is quantitative, showing self-consistency with the fit of the theory in Fig. 4.

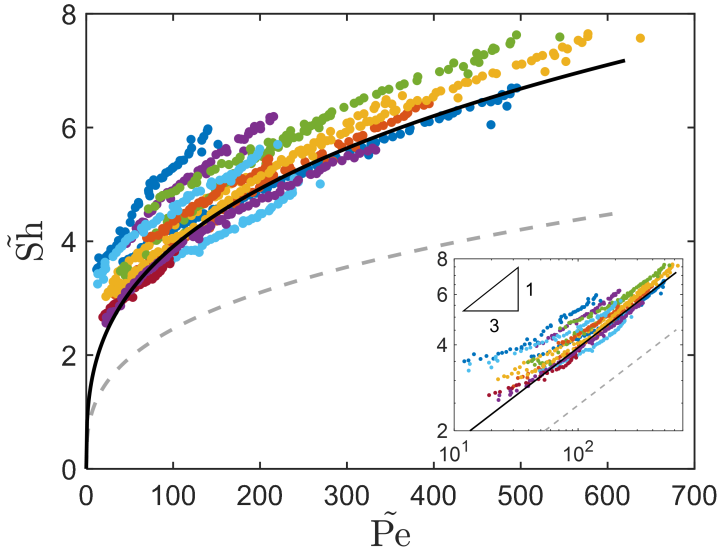

图 5. Effective Sherwood number vs effective Péclet number. The inset displays the data in a log-log format. Symbols: experimental data, corrected by their factors β_a and β_b computed as explained in the text after Eq. (10-12). The colours correspond to different runs. Gray dash line: uncorrected theory. Black solid line: theory accounting for averaged correction factors.

V. CONCLUSION

We have investigated the dissolution of an almost spherical particle during its sedimentation, in the low Reynolds and high Péclet regime. We use butyramide particles sedimenting in aqueous solution so that the density contrast between the particle and the solution is small, and thus the sedimentation velocity. The advantage of butyramide is that the density of its saturated solution is very close to the one of water, i.e. the dissolution does not affect the density of the solution.

The particle sediments in a squared tube, where a saturated butyramide layer is placed on top of a NaCl layer. The role of the top layer is to measure the sedimentation of the particle without dissolution and to have time to focus on the particle. The shape and the position of the particle are measured simultaneously by a camera attached to a translation stage. The particle is tracked in real time, and the translation stage moves accordingly to keep the particle in the field of the camera.

We develop a simple model for a perfect sphere based on Stokes' law (hypothesis of low Reynolds number) and the mass transfer at low Reynolds and high Péclet derived in [13]. We obtain a radius shrinking rate $\dot{a}$ which is constant in time, and only depends on the properties of the solid and the aqueous solution. The position of the particle is a third order polynomial of the time t. In the experiment, we define an equivalent radius from the image of the particle. We find as expected by the simple model that $\dot{a}$ is constant in time, and independent of the initial radius of the particle. Moreover, the theoretical and experimental results are consistent within 20% without any adjustable parameter.

In order to obtain an even more quantitative agreement, we introduce two correction factors: one to take into account the non-sphericity of the particle in the evaluation of its volume and weight (β_a), and a correction of the density of the particle due to the inclusions of air bubbles inside the particle (β_b). The non-sphericity of the particle and the inclusion of air bubbles are visible on the images. These two correction factors are close to one ($\beta_a = 0.921 \pm 0.002$ and $\beta_b = 0.988 \pm 0.002$). With these corrections, both the radius shrinking rate deduced from the equivalent radius and the one deduced from the particle trajectory are in quantitative agreement with the corrected model. We discuss other correction factors, such as the correction of the drag due to the non-sphericity of the particle, the correction of the mass transfer due to the non-sphericity, the finite solubility and non-isothermal effects in the dissolution of butyramide. We have shown that these corrections factors have a negligible effect in the present experiment, in contrast with β_a and β_b. Finally, we have defined an effective Sherwood number $\tilde{\mathrm{Sh}}$ and an effective Péclet number $\tilde{\mathrm{Pe}}$, and we have displayed the corresponding curve, which shows the $\tilde{\mathrm{Sh}} \propto \tilde{\mathrm{Pe}}^{1/3}$ scaling.

VI. ACKNOWLEDGEMENT

We gratefully acknowledge X. Benoit-Gonin, A. Fourgeaud and L. Quartier for technical support and A. Limare for technical help and scientific discussions. N.H. and Y.C. have been funded by Chinese Scholarship Council Scholarship.

[1] W. L. McCabe, J. C. Smith, and P. Harriott, *Unit operations of chemical engineering* (McGraw-HiII, 1993).
[2] P. Fryer, D. Pyle, and C. Rielly, *Chemical Engineering for the Food Industry* (Springer, 1997).
[3] H. Grijseels, D. J. A. Crommelin, and C. J. de Blaey, Hydrodynamic approach to dissolution rate, Pharmaceutisch weekblad **3**, 1005 (1981).
[4] A. Dokoumetzidis and P. Macheras, A century of dissolution research: From noyes and whitney to the biopharmaceutics classification system, International Journal of Pharmaceutics **321**, 1 (2006).
[5] P. Mcleod, D. S. Riley, and R. S. J. Sparks, Melting of a sphere in hot fluid, Journal of Fluid Mechanics **327**, 393–409 (1996).
[6] B. Qaddah, J. Monteux, and M. Le Bars, Thermal evolution of a metal drop falling in a less dense, more viscous fluid, Physical Review Fluids **5**, 053801 (2020).
[7] A. Chouippe, M. Krayer, M. Uhlmann, J. Dušek, A. Kiselev, and T. Leisner, Heat and water vapor transfer in the wake of a falling ice sphere and its implication for secondary ice formation in clouds, New Journal of Physics **21**, 043043 (2019).
[8] M. Vahab, D. Murphy, and K. Shoele, Fluid dynamics of frozen precipitation at the air–water interface, Journal of Fluid Mechanics **933**, A36 (2022).
[9] Q. Kriaa, E. Subra, B. Favier, and M. Le Bars, Effects of particle size and background rotation on the settling of particle clouds, Physical Review Fluids **7**, 124302 (2022).
[10] J. Philippi, M. Berhanu, J. Derr, and S. Courrech du Pont, Solutal convection induced by dissolution, Physical Review Fluids **4**, 103801 (2019).
[11] C. So, P. Chiang, and C. Mao, Modeling drug dissolution in 3-dimensional space, Pharmaceutical Research **39**, 907 (2022).

[12] S. Zhang and E. J. Davis, Mass transfer from a single micro-droplet to a gas flowing at low Reynolds number, Chemical Engineering Communications **50**, 51 (1987).

[13] V. G. Levich, *Physicochemical Hydrodynamics* (Prentice-Hall, Englewood Cliffs, 1962).

[14] R. Clift, J. Grace, and M. Weber, *Bubbles, drops and particles* (Academic Press, 1978).

[15] M. Assunção, M. Vynnycky, and K. M. Moroney, On the dissolution of a solid spherical particle, Physics of Fluids **35**, 053605 (2023).

[16] S. S. Kutateladze, V. E. Nakoryakov, and M. S. Iskakov, Electrochemical measurements of mass transfer between a sphere and liquid in motion at high Péclet numbers, Journal of Fluid Mechanics **125**, 453–462 (1982).

[17] J. M. Lawson and B. Ganapathisubramani, Mechanisms of mass transfer to small spheres sinking in turbulence, Journal of Fluid Mechanics **954**, A15 (2023).

[18] A. Lochiel and P. Calderbank, Mass transfer in the continuous phase around axisymmetric bodies of revolution, Chemical Engineering Science **19**, 471 (1964).

[19] B. Melissari and S. A. Argyropoulos, Development of a heat transfer dimensionless correlation for spheres immersed in a wide range of Prandtl number fluids, International Journal of Heat and Mass Transfer **48**, 4333 (2005).

[20] S. Petrescu, J. Petrescu, and C. Lisa, Mass transfer at solid dissolution, Chemical Engineering Journal **66**, 57 (1997).

[21] R. L. Steinberger and R. E. Treybal, Mass transfer from a solid soluble sphere to a flowing liquid stream, AIChE Journal **6**, 227 (1960).

[22] Y. L. Hao and Y.-X. Tao, Heat transfer characteristics of melting ice spheres under forced and mixed convection, Journal of Heat Transfer **124**, 891 (2002).

[23] J. M. Huang, M. N. J. Moore, and L. Ristroph, Shape dynamics and scaling laws for a body dissolving in fluid flow, Journal of Fluid Mechanics **765**, R3 (2015).

[24] N. Machicoane, J. Bonaventure, and R. Volk, Melting dynamics of large ice balls in a turbulent swirling flow, Physics of Fluids **25**, 125101 (2013).

[25] T. B. Oehmke and E. A. Variano, A new particle for measuring mass transfer in turbulence, Experiments in Fluids **62**, 16 (2021).

[26] A. Richter and P. A. Nikrityuk, Drag forces and heat transfer coefficients for spherical, cuboidal and ellipsoidal particles in cross flow at sub-critical Reynolds numbers, International Journal of Heat and Mass Transfer **55**, 1343 (2012).

[27] N. Kishore and S. Gu, Momentum and heat transfer phenomena of spheroid particles at moderate Reynolds and Prandtl numbers, International Journal of Heat and Mass Transfer **54**, 2595 (2011).

[28] C. Ke, S. Shu, H. Zhang, H. Yuan, and D. Yang, On the drag coefficient and averaged nusselt number of an ellipsoidal particle in a fluid, Powder Technology **325**, 134 (2018).

[29] Y. Chen, P. Jiang, T. Xiong, W. Wei, Z. Fang, and B. Wang, Drag and heat transfer coefficients for axisymmetric nonspherical particles: A LBM study, Chemical Engineering Journal **424**, 130391 (2021).

[30] T. Kiwitt, K. Fröhlich, M. Meinke, and W. Schröder, Nusselt correlation for ellipsoidal particles, International Journal of Multiphase Flow **149**, 103941 (2022).

[31] T. Elperin and A. Fominykh, Effect of solute concentration level on the rate of coupled mass and heat transfer during solid sphere dissolution in a uniform fluid flow, Chemical Engineering Science **56**, 3065 (2001).

[32] J. Magnaudet and M. J. Mercier, Particles, drops, and bubbles moving across sharp interfaces and stratified layers, Annual Review of Fluid Mechanics **52**, 61 (2020).

[33] Sommerfeld Arnold, *Optics*, Lectures on Theoretical Physics (Academic press, New York, 1954).

[34] Quaranta Lucien, *Dictionnaire de physique expérimentale* (Éditions Pierron, Sarreguemines, 2002).

[35] C. M. Romero and M. E. González, Solubility of acetamide, propionamide, and butyramide in water at temperatures between (278.15 and 333.15) K, Journal of Chemical & Engineering Data **55**, 2326 (2010).

[36] C. Gary-Bobo and H. W. Weber, Diffusion of alcohols and amides in water from 4 to 37.deg., The Journal of Physical Chemistry **73**, 1155 (1969).

[37] A. M. de Oliveira Siqueira, G. L. Chaves, J. de Souza Tanure, L. V. Dutra, N. B. de Souza, and T. C. Vianna, Determination of the diffusion coefficient in sodium chloride solution at different concentrations, The Journal of Engineering and Exact Sciences **8**, 14053 (2022).

[38] E. Loth, Drag of non-spherical solid particles of regular and irregular shape, Powder Technology **182**, 342 (2008).

[39] T. Darnige, N. Figueroa-Morales, P. Bohec, A. Lindner, and E. Clément, Lagrangian 3D tracking of fluorescent microscopic objects in motion, Review of Scientific Instruments **88**, 055106 (2017).

[40] J. A. Balderas-López, A. Mandelis, and J. A. Garcia, Thermal-wave resonator cavity design and measurements of the thermal diffusivity of liquids, Review of Scientific Instruments **71**, 2933 (2000).